Altered drug metabolism and increased susceptibility to fatty liver disease in an inducible liver-specific mouse model of myotonic dystrophy

Zac Dewald[1], Ullas V. Chembazhi[1], Andrew Gupta[1], and Auinash Kalsotra[1,2,3§]

[1]Department of Biochemistry, [2]Cancer Center@Illinois, and [3]Carl R. Woese Institute for Genomic Biology, University of Illinois, Urbana-Champaign, IL, United States.

[§]To whom correspondence should be addressed. E-mail: kalsotra@illinois.edu

Phone: 1-217-300-7654

Fax: 1-217-244-5858

Running title: Fatty liver disease and drug metabolism defects in DM1

Keywords: Myotonic dystrophy type 1, Alternative splicing, RNA toxicity, Mouse model, Fatty liver disease, Drug metabolism

Abstract

Myotonic Dystrophy type 1 (DM1) is multi-systemic muscular dystrophy, affecting 1 in 3000 people, characterized by muscle wasting, myotonia, cardiac and gastrointestinal abnormalities and cognitive impairment, among other symptoms. DM1 is caused by a (CTG)n repeat expansion in the 3' UTR of the ubiquitously expressed gene *DMPK*. The (CUG)n containing RNAs resulting from the transcription of this diseased *DMPK* gene aggregate in the nucleus, forming foci which sequester muscleblind-like (MBNL) family proteins, a group of splicing factors that play significant roles in the juvenile-to-adult development of many tissues. Recent studies show that DM1 patients have increased susceptibility toward glucose intolerance, non-alcoholic fatty liver disease (NAFLD), and metabolic syndrome. Furthermore, DM1 patients are abnormally sensitive to a wide range of analgesics and anesthetics, with complications ranging from prolonged anesthesia recovery to heightened pulmonary dysfunction. These findings suggest a predisposition for liver damage and dysfunction in DM1 patients; however, this possibility has gone uninvestigated. To understand the effects of DM1 in the liver, we generated a hepatocyte-specific DM1 mouse model in which we can induce the expression of CUG containing RNA, specifically in the liver. Through these mice, we demonstrate that the expression of the toxic RNA in hepatocytes sequesters MBNL proteins, causing a reduction in mature hepatocellular activity, however, we find that, in contrast to other tissues, loss of MBNL1 activity only reproduces a small portion of the transcriptome changes in DM1 afflicted hepatocytes. We characterized the transcriptomic changes driven by DM1 in the liver and show that these lead to changes in hepatocellular morphology, inflammation, and necrosis, as well as excessive lipid accumulation and fatty liver disease. We further demonstrate that DM1 mice livers are

defective in drug metabolism and clearance, and when challenged, exhibit marked impairment against zoxazolamine-induced paralysis and acetaminophen-induced hepatotoxicity. Together, these results reveal that the expression of CUG repeat containing RNA disrupts the normal hepatic functions and predisposes the liver to injury, fatty liver disease, and drug clearance pathologies that may jeopardize the health of DM1 patients and complicate the treatment of DM1.

Introduction

Myotonic Dystrophy Type 1 (DM1) is an autosomal dominant disease and the second most common form of muscular dystrophy, affecting more than one in three thousand adults in North America (Ashizawa et al., 2018; Harper, 2003). The cardinal symptoms of DM1 include myotonia, debilitating muscle weakness and wasting, abnormal heart function, and excessive fatigue (Ashizawa et al., 2018; Harper, 2003). Despite DM1's initial characterization as a form of muscular dystrophy, the disease is genuinely multisystemic; patients report various gastrointestinal, metabolic, and neurological dysfunctions, such as excessive daytime sleepiness and insulin resistance (Ashizawa et al., 2018; Heatwole et al., 2012).

DM1 is caused by a (CTG)n repeat expansion in the 3' UTR of a ubiquitously expressed gene Dystrophia Myotonica protein kinase (*DMPK*) (Brook et al., 1992; Day & Ranum, 2005; J. E. Lee & Cooper, 2009). The (CUG)n containing RNAs resulting from the transcription of the diseased *DMPK* gene form hairpin secondary structures and aggregate in the nucleus, forming discrete RNA foci (J. E. Lee & Cooper, 2009; Mankodi, 2000). These foci interact with and sequester the muscle blind-like (MBNL) family of splicing factors (Jiang et al., 2004; Miller, 2002). MBNL proteins affect many developmentally-regulated alternative splicing and polyadenylation decisions in various tissues throughout the process of maturation towards adulthood; thus, their loss-of-activity in DM1 shifts splicing of target pre-mRNAs towards fetal-like patterns, inducing specific features of the disease(Chau & Kalsotra, 2015; Ho et al., 2004; Lin et al., 2006; Wang et al., 2012). This reversal of transcriptomic patterning from fully mature to a more immature state causes many of the disease symptoms to become more prevalent later in life, with diagnosis often occurring in

the mid to late 30's (Lin et al., 2006; Philips et al., 1998; Yum et al., 2017). However, diagnosis typically occurs only after the development of significant muscular or neurological symptoms, which allows for the subtle and long-term consequences of the disease to go un-managed (Turner & Hilton-Jones, 2010).

DM1 patients are abnormally sensitive to a wide range of anesthetics and muscle relaxants, resulting in prolonged anesthesia recovery, heightened pulmonary dysfunction, and in some cases, death (Campbell et al., 2010; Harper, 2003; Mathieu et al., 1997). Often, these symptoms are attributed to the disruption of neurological and muscular function, which is a hallmark of DM1. However, within the last twenty years, several studies have demonstrated that DM1 patients have an increased susceptibility to non-alcoholic fatty liver disease (NAFLD), metabolic syndrome, and liver damage (Achiron et al., 1998; Bhardwaj & Duchini, 2010; John Herbick, 2013; Shieh et al., 2010). These studies would suggest inappropriate liver function and a predisposition for liver injury in DM1 patients. A malfunctioning liver could also help explain the sensitivity to anesthetic treatment; a liver that is unable to provide adequate metabolism of xenobiotic material would prolong the clearance time for many drugs and may increase their potency. Minor malfunctions in liver response to metabolic signaling and drug metabolism may indeed be a frequent occurrence in DM1 patients; however, none have investigated this possibility.

Here we sought to determine what effects DM1 might have upon liver function and overall liver health. Utilizing two previously established mouse lines, we generated a mouse model in which we induced the expression of (CUG)n repeat-containing RNA, specifically in the hepatocytes within the liver (J. Lee et al., 2019; Morriss et al., 2018; Xu et al., 2005). Utilizing a combination of biochemical, molecular, and computational methods, we found that

expression of the toxic (CUG)n RNA triggered global gene expression and RNA processing defects in the hepatocytes. These transcriptome defects led to a variety of physiological and cellular pathologies, including accumulation of lipids and fatty liver, increased susceptibility to insult and injury, and misregulation of xenobiotic metabolism. However, in contrast to some other tissues, it appears that the ablation of MBNL1 activity alone is not sufficient to replicate the effects of DM1 within the liver. Thus, our results reveal that DM1 disrupts the normal hepatic functions and predisposes the liver to fatty liver disease and injury and confirms the need for increased research into the effects of DM1 in non-traditional tissues, including the liver.

Results

A hepatocyte-specific murine model of DM1 recapitulates the molecular features of the disease in the liver

The pathogenic mechanism of DM1 is comprised of three primary parts: i) the transcription and production of a long CUG repeat-containing RNA, ii) the accumulation of this RNA into nuclear foci, and iii) the sequestration of MBNL proteins into such RNA foci, which results in the decrease of MBNL directed RNA processing activities (Machuca-Tzili et al., 2005; Scotti & Swanson, 2016; Wheeler & Thornton, 2007). To study the effects of DM1 within the liver, we generated a bi-transgenic murine model by combining two existing mice models. First, is the tetracycline-inducible mouse model with a *DMPK* transgene containing the last five exons of human *DMPK* and 960 interrupted CTG repeats (labeled here as CUG960i RNA), developed by Cooper and colleagues (Morriss et al., 2018). The second model utilizes the expression of a reverse tetracycline trans-activator (rtTA) driven by the apolipoprotein E (ApoE) promoter, which is highly expressed in the hepatocytes of the liver (Xu et al., 2005). By crossing these two mice models we generated a double homozygous bi-transgenic line that allows for conditional, doxycycline (Dox)-dependent expression of the CUG960i RNA specifically in the liver tissue, thus allowing the study of DM1 disease in the liver (**Fig. 1A**). From now on this bi-transgenic model is referred to as the DM1 liver model, and the control mice for this model contain only the homozygous ApoE-rtTA allele.

To mimic the DM1 conditions seen in human patients, we induced the disease in newborn pups by feeding the mother a diet supplemented with 2 g of Dox per kg of

chow. Once weaned, mice then continued a Dox diet at a lower dose of 0.1 g/kg until they reached adulthood, occurring roughly at nine weeks (**Fig. 1B**). At eight weeks of age, mice fasted for 20-22 hours were administered a glucose tolerance test (GTT), where mice received 2 mg of glucose per g of body weight via intraperitoneal injection (IP) and glucose levels were monitored periodically for 2 hours.

To confirm the appropriate expression of the CUG960i RNA and the formation of toxic RNA/RNA binding protein (Rbp) foci, we utilized fluorescent in-situ hybridization and immunofluorescence (FISH-IF) with probes targeting the CUG repeat sequence within the RNA (**Fig. 1C**). Bright puncta of condensed CUG RNA were seen in the nuclei of most hepatocytes, and, notably, these RNA foci overlapped with a fluorescent signal when either anti-MBNL1 or MBNL2 antibodies were used, indicating that the toxic CUG RNAs have successfully sequestered the MBNL proteins. The MBNL containing RNA foci only occurred in the DM1 mice livers and not in the ApoE-rtTA control mice livers. Quantification of the CUG960i/MBNL foci indicated that over 80% of hepatocyte nuclei in the DM1 mice contain at least one RNA focus, ensuring the uniformly distributed expression of both transgenes (**Fig. 1D**). The appearance of RNA foci was Dox-dependent — when mice with both the ApoE-rtTA and CUG960i alleles are either not fed Dox or if the Dox diet was withdrawn for a week or more, the RNA foci were undetectable. The distribution of CUG960i RNA foci per nuclei followed a Poison curve, with most hepatocytes having one to three foci and a small number of hepatocytes exceeding ten plus foci within a single nucleus (**Fig. 1E**).

Finally, to assay the amount of toxic RNA produced, CUG960i transgene expression was quantified by extracting RNA from whole livers and performing quantitative PCR

(qPCR) with primers located in the final exon of *DMPK* transcript. DM1 liver mice expressed the CUG960i transgene at levels near those of β-actin transcripts within the liver, compared to ApoE-rtTA control mice, which showed no evidence of CUG960i expression (**Fig. 1F**). A comparison of CUG960i RNA within isolated hepatocytes versus that of the whole liver confirmed that the transgene's expression occurs primarily within hepatocytes (**Fig S1A, B**). Livers of the bi-transgenic mice not fed Dox showed little evidence of CUG960i expression, confirming that Dox must be fed to these animals to express sufficient amounts of toxic RNA. (**Fig. 1F**).

Expression of CUG960i RNA induces global transcriptomic changes within hepatocytes

Upon establishing that the DM1 liver model reproduces the molecular features of the disease, we prepared total RNAs from purified hepatocytes isolated from the ApoE-rtTA controls and DM1 afflicted mice livers that were fed a 2.0 g/kg Dox-supplemented diet for nine weeks. We next tested the splicing patterns of MBNL1-regulated exons within these RNA samples using end-point reverse-transcription PCR (RT-PCR) assays. The DM1 mouse livers consistently reproduced an alternative splicing pattern that significantly deviates from the control samples (**Fig. 2A**), confirming that like the muscle and brain tissues, the expanded CUG repeat containing RNA of DM1 also induces splicing defects in the liver. We performed high-resolution RNA-sequencing of poly(A) selected RNA from the purified hepatocyte samples to further explore the genome-wide RNA processing defects in DM1 afflicted livers. Analysis of the resulting data revealed

widespread changes in the DM1 hepatocyte transcriptome, with significant changes in mRNA abundance, splicing, and alternative polyadenylation (ApA) (**Fig. 2B**). Focusing upon the gene expression, inducing DM1 within the murine liver changed the mRNA abundance of 760 transcripts at a 2-fold level or higher, 516 upregulated and 244 downregulated compared to control livers (**Fig. 2C**).

As the MBNL proteins are most known for regulating alternative splicing events, it is not surprising that nearly one thousand splicing events change upon the expression of the toxic DM1 RNA within the liver. Of the splicing 928 splicing events which demonstrate a greater than 10% change in PSI (Percent Spliced In) within the DM1 liver, every form of alternative splicing is represented, with most of the events falling under the category of cassette exons, with 35 of these events showing a ΔPSI change of 50% or higher (**Fig. 2D, S1C**). Forty-one of these alternatively spliced events were validated by RT-PCR; the comparison showed a high consistency between the RNA-seq and RT-PCR results (**Fig. 2F**).

Gene ontology analysis of the transcripts with dysregulation in abundance, splicing or ApA revealed enrichments in unique functional categories. Transcripts changing in abundance were enriched in glucose, lipid and energy-related metabolism, as well as oxo-reductase and cytochrome p450 activity (**Fig. 2I, Table 1**)(Huang et al., 2007, 2009). The transcripts with altered splicing patterns were however enriched in mRNA processing, signal transduction and protein phosphorylation. A substantial number of transcripts encoding proteins associated with the immune response, specifically response to viral and bacterial infection, exhibited defects in both overall abundance and splicing (**Fig. 2J, Table 2**). Transcripts with misregulated ApA events, much like

misregulated splicing events, were enriched in nucleotide binding, protein binding and transport-related functions.

The proposed molecular mechanism of DM1 entails the disruption of MBNL protein activities, resulting in a transcriptomic shift away from the normal state of healthy adult tissue and towards an immature state in the muscles, heart, and neurons (Chau & Kalsotra, 2015; Scotti & Swanson, 2015; Sobczak et al., 2014; Wang et al., 2019; Wheeler & Thornton, 2007). To test whether this pattern holds within the liver, we isolated hepatocytes from *Mbnl1*$^{\Delta E3/\Delta E3}$ (*Mbnl1* knockout) mice at ten weeks of age and corresponding littermate wild-type controls (Kanadia, 2003). Again RT-PCR splice assays, and RNA-seq were performed on the poly(A) selected RNAs purified from freshly isolated wildtype and *Mbnl1* KO hepatocyte samples and the results compared to the DM1 liver and ApoE control samples as previously mentioned. Notably, the DM1 liver samples showed a shift in splicing away from controls in the same direction as the *Mbnl1* KO samples (**Fig. 2F, S1D, E**). However, it is also interesting to note that the DM1 samples often demonstrate a more significant deviation from “normal” than the *Mbnl1* KO samples.

As MBNL proteins play a role in regulating mature liver development and function, we compared the transcriptomic changes in the DM1 liver versus those changing in either the *Mbnl1* KO model or during postnatal liver maturation (Bangru et al., 2018). By comparing alternatively spliced transcripts that change in either the context of DM1, *Mbnl1* knockout, or in liver maturation, we found that only about 25% of the events changing in DM1 were regulated by MBNL1 (**Fig. 2G, H**). Of note, whereas only a modest portion of misspliced events in DM1 were developmentally regulated, over 50%

of transcripts changing in abundance in the DM1 liver were also developmentally regulated.

Hepatocyte-specific expression of CUG960i RNA induces increased lipid accumulation and liver injury

As the effects of DM1 in the liver are largely unstudied, and even the role of MBNL proteins in the liver are unknown, we took a generalized approach to assess the pathological consequences of DM1 within the liver. This process started before sacrifice, as blood glucose levels just before sacrifice indicate a slight difference in the blood glucose levels between male DM1 liver mice and male controls (**Fig. 3A**). However, this difference does not occur within the female groups (**Fig. S2A**). There was also no difference between DM1 liver mice and controls during glucose tolerance testing performed in the weeks before sacrifice (**Fig. 3B, S2B**). Median mouse weight between control and DM1 mice showed no significant difference (**Fig. S2C**).

As glucose intolerance is a common symptom in DM1, we compared GTT analysis from the DM1 liver mice and control mice against a DM1 mouse model commonly studied for skeletal muscle pathologies, the HSA L/R model (Mankodi, 2000). The HSA L/R model expresses the toxic CUG repeat containing RNA only within the muscle tissues, allowing us to compare the direct contributions of liver and muscle tissue towards glucose intolerance in DM1. Interestingly, while the HSA L/R mice showed a significant degree of glucose intolerance, the DM1 liver mice were normal in their glucose handling (**Fig 3B**).

Histological analysis of the DM1 mice livers using Hematoxylin and Eosin (H&E) staining revealed varying degrees of morphological changes and regions with decreased sinusoidal spacing within the DM1 livers (**Fig 3C**). Additionally, increased lobular inflammation and necrotic patches were found within the DM1 livers (**Fig. 3C**). DM1 patients have shown an increased susceptibility to fatty liver disease (Bhardwaj & Duchini, 2010; Shieh et al., 2010), therefore, we used Oil Red O staining on frozen mice liver tissues to interrogate the lipid accumulation within the DM1 liver model. Relative to the control animals, DM1 liver mice showed a significant increase in lipid droplets (**Fig. 3C, D**). While a long-term Dox diet can result in a modest accumulation of lipids in the liver, the DM1 mice consistently displayed higher lipid levels nearly twice that of respective controls. Furthermore, the mouse liver to carcass weight ratio showed a significantly higher hepatosomatic index in DM1 liver mice than that of respective controls (**Fig. 3E**), with a median increase of 36.6%.

DM1 murine liver models are more susceptible to fatty liver disease and injury

As DM1 patients face dietary and mobility challenges that often require counseling and careful monitoring, we set out to test if the macronutrient composition of the patient diet impacts the DM1 liver's susceptibility to NAFLD (Ashizawa et al., 2018; Heatwole et al., 2012; Savkur et al., 2001; Chris Turner & Hilton-Jones, 2010). To do so, we fed DM1 liver mice, and ApoE-rtTA controls normal chow supplemented with a 2 g/kg Dox diet until weaning as previously described. Once weaned, the mice were switched to a high-fat, high-sugar, and heightened cholesterol (western) diet supplemented with 0.1 g/kg

Dox for a total of eight additional weeks (**Fig. 5a**) (Elmgren et al., 2007; Escolà-Gil et al., 2011). As before, we analyzed GTT and four-hour fasted glucose levels before sacrifice.

GTT analysis again showed no difference between DM1 mice and control animals (**Fig. 5B**); however, there was a slight difference in 4 hour fasted blood glucose levels between male DM1 and male control mice (**Fig. 5C**). In reverse of the basal diet, DM1 mice had significantly lower blood glucose.

While control livers turned pale following a high fat, high sugar diet, the DM1 livers became exceedingly lighter, with much of the usual red color replaced with off-white due to excess lipid accumulation (**Fig 5D**). Both DM1 and control mice showed significant increases in micro-and macro-vesicular steatosis, inflammation, and evidence of cell death on the western diet compared to the regular rodent diet (**Fig. 5D**). However, DM1 mice showed much greater steatosis, patchy necrosis as well as ballooning and feathery degeneration after western diet feeding. Oil Red O staining showed that livers of DM1 mice had a much higher density of lipid droplets as well as a significant increase in the number of large lipid droplets (**Fig. 5D**), making them challenging to quantify via image analysis. Therefore, we used an alternative method to determine the relative accumulation of lipids in the western diet-fed control and DM1 mice. A hexane/isopropanol lipid extraction protocol was used to collect hydrophobic fatty acids from small liver portions. A colorimetric assay for triglycerides was performed upon these extracts (**Fig. 5E**). This analysis revealed two interesting features. First, the livers from DM1 mice fed the regular rodent diet accumulated as many triglycerides as the

livers from control mice on the western diet. Second, the livers of DM1 mice fed a western diet accumulated significantly more triglycerides than any other group. Western diet fed DM1 mice also had a more significant increase in liver to body weight ratios than controls (**Fig. 5F**). The mean body weight between DM1 and control mice is invariant, suggesting that the increase accumulation of lipids in the liver is not due to a greater increase in body weight (**Fig. S2E**).

DM1 liver model mice demonstrate decreased drug metabolism

An often-reported challenge when treating DM1 patients is that they demonstrate increased susceptibility to anesthetics and analgesics (Ashizawa et al., 2018; Campbell et al., 2010; Veyckemans & Scholtes, 2013). These complications are most noticeable during surgical procedures wherein DM1 patients exhibit much longer recovery times from various anesthetics and muscle relaxants. In the case of a few anesthetics, the patient may require intervention to prevent death (Groh et al., 2008; Mathieu et al., 1997). Because liver is the primary organ involved in drug metabolism, we hypothesized that DM1 livers might be compromised in responding to and metabolizing xenobiotics, thereby decreasing DM1 patients' ability to clear certain drugs from their system. We first chose zoxazolamine, a muscle relaxant, to test this hypothesis. Zoxazolamine testing in mice consists of inducing muscle paralysis in the animals via zoxazolamine injection and then monitoring them until they can self-right and move around freely (**Fig. 6A**). Zoxazolamine metabolism generally shows a sex-specific response in mice;

however, in both males and females, DM1 mice took at least 50% longer to recover from the drug-induced paralysis (**Fig. 6B**).

We next tested if a similar reduction in drug metabolism occurred with common, over-the-counter analgesics such as acetaminophen (APAP). APAP is hepatotoxic if consumed in high concentrations as it generates toxic levels of N-acetyl-p-benzoquinone imine (NAPQI) metabolite after oxidation by CYP2E1 in perivenous hepatocytes (James 2003) (**Fig 6C**). Even a low dose of APAP can induce liver toxicity if CYP2E1 activity is high, and conversely, the liver can be insulated from APAP toxicity if CYP2E1 activity is ablated (Zaher 1998). In mice, the LD50 of APAP is between 320 and 370 mg per kg of bodyweight when administered intraperitoneally (Craig 1980). To see if DM1 changed susceptibility to APAP-induced hepatic injury, we injected 350 mg of APAP per kg of body weight into fasted DM1 and control mice. Mice were monitored for 8 hours and then left to recover for an additional 16 hours before being sacrificed. A difference was immediately noticed between DM1 and control mice, as significantly more control mice died within the first 8 hours compared to DM1 mice (**Fig. 6D**). Upon collecting the liver from the surviving mice, 24 hours post-APAP injection, almost all control animals show widespread signs of liver necrosis (**Fig. 6E**). However, APAP-treated DM1 livers showed fewer instances of injury and necrosis (**Fig. 6E**). H&E staining of the APAP treated livers also showed marked differences between DM1 and control mice, with DM1 mice still showing extensive injury and hepatocyte vacuolization but far less necrosis. (**Fig. 6F**).

Discussion

Several reports have demonstrated that DM1 is a multisystemic disease, and that a variety of tissues demonstrate pathologies that affect patients' health (Brunner et al., 1992; Jiang et al., 2004; Machuca-Tzili et al., 2005). In this study, we have demonstrated that the liver is one of the many organs negatively affected by DM1.

Previous work has demonstrated that MBNL proteins are upregulated within the hepatocytes as the liver matures after birth (Bhate et al., 2015). We have shown here that the mechanism by which DM1 affects the liver is to inhibit not only MBNL1 but also MBNL2 and other splicing factors as they work to reinforce a pattern of splicing that allows the liver to perform mature functions. Inhibition of these splicing factors leads to various consequences, including increased lipid accumulation, improper regulation of CYP450 activity, and increased susceptibility to hepatocellular injury. These cellular defects, in turn, lead to more gross pathologies, including a propensity towards fatty liver disease, hepatic necrosis, and susceptibility to injury from toxins and dietary stress.

In conclusion, we have demonstrated that MBNL1 and MBNL2 serve essential roles in facilitating mature liver activity. The sequestration of these proteins by toxic CUG repeat containing RNAs produced in DM1 causes a global RNA processing and gene expression defects, inhibiting these abilities. These findings in part explain the previous reports of increased fatty liver disease and metabolic disorders in DM1 patients ((Achiron et al., 1998; Bhardwaj & Duchini, 2010; Shieh et al., 2010)). Our work also highlights the importance of continued research into what role the liver plays in the general metabolic disruption drug sensitivities in DM1 patients and what role the liver might play in contributing to the unique susceptibility DM1 patients display towards specific muscle

relaxants and anesthetics. In conclusion, we have demonstrated that MBNL1 and MBNL2 serve essential roles in facilitating mature liver activity. The sequestration of these proteins by toxic CUG repeat containing RNAs produced in DM1 causes a global RNA processing and gene expression defects, inhibiting these abilities. These findings in part explain the previous reports of increased fatty liver disease and metabolic disorders in DM1 patients (Achiron et al., 1998; Bhardwaj & Duchini, 2010; Shieh et al., 2010). Our work also highlights the importance of continued research into what role the liver plays in the general metabolic disruption and drug sensitivities in DM1 patients and what role the liver might play in contributing to the unique susceptibility DM1 patients display towards specific muscle relaxants and anesthetics.

ACKNOWLEDGEMENTS

Work in the Kalsotra laboratory is supported by National Institute of Health (R01HL126845, R01AA010154), Muscular Dystrophy Association (MDA514335), and the Beckman Fellowship from the Center for Advanced Study at the University of Illinois Urbana-Champaign. Z.D. was supported by the NIH Chemistry–Biology Interface training program (T32-GM070421). U.V.C. was supported by the Herbert E. Carter fellowship in Biochemistry. A.G. was supported by the Jenner Family Summer Research Fellowship. We acknowledge support from the Transgenic mouse core, High-throughput sequencing and genotyping core and Histology-microscopy core facilities at the University of Illinois, Urbana-Champaign.

AUTHOR CONTRIBUTIONS

Z.D., and A.K. conceived the project and designed the experiments. Z.D., U.V.C. and A.G. performed experiments and analyzed the data. Z.D. and A.K. interpreted results and wrote the manuscript. All authors discussed the results and edited the manuscript.

COMPETING INTERESTS

The authors declare no competing financial interests.

RESOURCE AVAILABILITY

Lead Contact

Requests for reagents, resources and/or additional information should be directed to the corresponding author, Auinash Kalsotra (kalsotra@illinois.edu).

Materials Availability

Please contact corresponding author for materials or resources generated in this study

Materials and Methods

Mouse Models

National Institutes of Health (NIH) and University of Illinois, Urbana-Champaign (UIUC) institutional guidelines were followed in the use and care of laboratory animals. All experimental protocols were performed as approved by the Institutional Animal Care and Use Committee. The study is not gender-specific and specimens include both male and female animals; however, as attributes such as glucose regulation and body weight are sex specific, animal sex was always recorded. Whole liver tissues and hepatocytes were isolated from mice following guidelines for euthanasia and/or anesthesia.

Four mouse models were utilized in this study. First, the control animals used for the DM1 experiment, the ApoE-rtTA mice, were a mixed strain C57Bl6/DBA mouse line, with a single transgene containing a reverse tetracycline TransActivator (rtTA), expressed under the ApoE promoter (Xu et al., 2005). Second, the “DM1 liver” line, was also a mixed strain line, combining FVB background TRE-960i mice with the ApoE-rtTA mice. The resulting FVB/C57Bl6/DBA mice contained both the ApoE-rtTA transgene as well as tetracycline response element (TRE) driven truncated DMPK gene containing only the last 5 exons of human DMPK (Morriss et al., 2018). The DMPK construct also contained an elongated CUG repeat sequence, with a total of 960 repeats. These repeats are interrupted every 20 repeats with a “ctcga” sequence to prevent the overall repeat sequence from undergoing expansion or shrinkage. Both the ApoE-rtTA mice and DM1 liver mice maintained as homozygotes for all transgenic alleles.

HSA L/R mice were FVB mice expressing a truncated human skeletal actin (HSA) with a ~240 CUG repeat sequence in the 3’ UTR of the transgene (Mankodi, 2000). The HSA was driven by the skeletal actin promoter, allowing for the expression of CUG repeats within the skeletal muscle tissue exclusively. The HSA L/R mice were maintained as homozygotes.

The final model, the *Mbnl1* knock out (KO) or *Mbnl1*$^{\Delta E3/\Delta E3}$ line was an FVB mouse where the 1st coding exon of *Mbnl1* has been replaced with a cassette using cre-lox insertion (Kanadia, 2003). This mouse line was maintained in the heterozygous state, and homozygous mutant (*Mbnl1*$^{\Delta E3/\Delta E3}$) or homozygous wildtype (*Mbnl1*$^{Wt/Wt}$) being generated for study or as controls when needed.

Diet Scheme

Both the DM1 liver and ApoE-rtTA mice were fed under the following scheme unless otherwise noted. To mimic the DM1 conditions seen in human patients, we induced the disease at birth, giving the mothers 2.0 g/kg doxycycline (Dox) supplemented Teklad 2018 18% protein global rodent diet; the Dox is transmitted through the mother's milk to the pups. The 2.0 g/kg Dox diet is continued until weening, which occurs at 21 days after birth.

For most experiments performed in this study, the diet of the mice was then switched to a 0.1 g/kg Dox supplemented Teklad 2018 global rodent diet and maintained on this diet until sacrifice at 9 weeks of age. Some important exceptions were the mice used for RNA-seq, which were maintained on a diet of 2 g/kg Dox supplemented diet until sacrifice at 9 weeks. Mice noted as "No-Dox" were fed only global rodent diet without Dox until sacrifice at 9 weeks. Mice noted as "Recovery" were fed 0.1g/kg Dox supplemented diet as normal, but then switched back to Dox free diet prior to sacrifice at 9 weeks of age.

Western Diet mice were fed as before, with the mothers being fed 2g/kg Dox supplemented chow until weening, at which point the mice were transitioned to a high fat, high sugar, cholesterol supplemented "western, purified atherogenic" Diet (Teklad 88137), supplemented with 0.1g/kg Dox. These mice were maintained on this diet for 8 weeks after weening, until being sacrificed at 11 weeks of age.

Glucose Tolerance Testing (GTT)

GTT was performed on male and female mice, either 7 days prior to sacrifice if they were maintained on the 0.1g/kg Dox diet, or at 10 and 5 days prior to sacrifice if they were on the

western diet. For both cases, GTT was performed after the mice were fasted for 24 hours. Glucose was injected through intraperitoneal injection (IP) at a concentration of 2 g/kg body weight. Tails were clipped, blood was collected, and glucose was measured, using a One Touch Ultra 2 glucose meter, after 0, 15, 30, 60, 90, and 120 minutes.

Sacrifice and tissue collection

Mice were fasted in the morning and were sacrificed after 4 to 6 hours of fasting. Liver and carcass weight were taken at the time of sacrifice, as well as 600 µL of blood via retro-orbital bleeding. During sacrificing, liver tissues were collected for (1) RNA, protein, and lipid isolation, (2) paraffin-embedding, and (3) cryo-sectioning. Tissue for cryo-sectioning was collected by sectioning two pieces of liver, embedding the tissues in Optimal Cutting Temperature (OCT) compound and frozen on dry ice. Tissues for paraffin embedding were stored in neutral buffered formalin for 48 hours before being stored in 70% ethanol until paraffin embedding. The remaining tissue was flash frozen in liquid nitrogen.

Isolation of Hepatocytes

Hepatocyte isolation was performed using two-step perfusion with centrifugal separation to produce a cell population highly enriched in hepatocytes; this population of cells was then used for RNA-seq analysis. The method for hepatocyte isolation was adapted from Li et al., 2010.

Briefly, mice were anesthetized in a chamber supplied with isoflurane and oxygen (2.5% isoflurane in oxygen, 1.5Lmin.). Mice were maintained on the anesthetic during the procedure via use of a nose cone. The liver was perfused via cannulation of the portal vein with 30-40 ml of a 1× HBSS (Hank's balanced salt solution) with phenol red (without Ca^{2+} and Mg^{2+}), 0.5 mM EDTA solution, at a flow rate between 3 and 5 mL per minute. This solution was then followed by 50 ml of a 1× HBSS (with Ca2+), 5.4 mM CaCl2, 0.04 mg ml−1 soybean trypsin inhibitor, and 3000 units of collagenase type I (Worthington Chemicals)). Subsequently, the liver was massaged in a Petri dish containing 1× HBSS with phenol red (without Ca^{2+} and Mg^{2+}), to

462 release cells from the liver capsule, and then the cell suspension was passed through a 70-μm
463 filter to obtain a single-cell suspension. The cells were then centrifuged at 50 × g for 5 min (4 °C)
464 to separate live hepatocytes from non-parenchymal cells and dead cells. The cells were further
465 washed 3 times in 1× HBSS as above, and then flash frozen in liquid nitrogen and stored at
466 −80 °C till further use.

467 *RNA Isolation and cDNA Synthesis*

468 Total RNA was isolated from either liver or from perfused hepatocytes via TRIzol
469 extraction. One milliliter of TRIzol was added to small pieces (approximately 30 μg to 50 μg) of
470 either liver or hepatocyte isolate. Lysing of the cells was hastened by homogenization of via
471 bullet blending with NextAdvanced Zirconium oxide 1mm beads. Chloroform was added and
472 the mixture was centrifuged for 10 minutes at 10,000xg which caused a separation of
473 layers. The aqueous layer, containing extracted RNA, was removed and to this was added 600
474 μL of isopropanol. The solution was then mixed and stored at -20℃ overnight (or for at least 8
475 hours). Afterwards, the mixture was centrifuged for 40 min at 12,000xg, causing the precipitation
476 of the RNA. The chloroform was removed, and the RNA pellet was washed with 70% ethanol.
477 The RNA was then dissolved in water. RNA purity and concentration were assessed with
478 a Biotek Synergy 2 UV spectrometer.

479 cDNA synthesis was performed on 1 μg of RNA, using random hexamer primers and
480 Maxima Reverse Transcriptase (from Thermo Scientific). The cDNA was diluted to a total
481 volume of 200 μL.

482 *RNA-seq*

483 RNA was isolated from experiment specific hepatocytes using RNeasy tissue mini-kit
484 (Qiagen). Prior to library preparation, RNA quality was assessed using an Agilent Bioanalyzer,
485 by the Functional Genomics Core at the Roy J. Carver Biotechnology Center, UIUC. Poly-
486 A selected, RNA-seq libraries preparation and 150-bp paired-end Illumina sequencing was
487 performed on a NOVASEQ 6000 at the High Throughput Sequencing and Genotyping Unit,

UIUC. RNA-seq reads were processed for quality and read length filters using Trimmomatic (version 0.39). RNA-seq reads were further aligned to the mouse genome (mm10) using STAR (version 2.5.2).

Gene expression levels were determined as TPM using count and differential expression values obtained from DESeq2 (version 1.8.2), Htseq (version 0.6.1) and Cuffdiff 2 (version 2.2.1) (Anders et al., 2015; Love et al., 2014; Trapnell et al., 2012). Genes were considered as having significant differential expression following imposed cutoff clearance (FDR $\leq$ 0.05, log2(fold change) $\geq$1). Differential splicing analysis was performed using rMATS (version 3.2.5), and significant events were identified using imposed cutoffs (FDR $\leq$ 0.10, junction read counts $\geq$ 10, PSI $\geq$ 10%) (Shen et al., 2014). Motif analysis for differentially spliced exons was performed using rMAPS with default parameters, and putative motifs as described previously (Park et al., 2016). To perform alternative poly adenylation (APA) analysis, 3'UTR expression quantification was performed via Salmon (version 1.0.0), followed by analysis via qAPA (version 1.2.2) (Ha et al., 2018; Patro et al., 2017). APA events were determined as being significant if there was a change of 5 TPM or greater. Gene ontology analysis was performed using DAVID (version 6.8) (Bonnot et al., 2019; Huang et al., 2007, 2009; Supek et al., 2011).

To perform the exon ontology analysis, exons undergoing significant changes in splicing were converted to corresponding human exons in the hg19 annotation using UCSCliftover with minimum ratio of bases matching as 0.8(Kent et al., 2002). Additionally, the exons in hg19 reported by UCSCliftover were checked for gene identity match to the mouse exon's parent gene. These exons were then analyzed for ontology using the exon ontology and FasterDB packages (Benoit-Pilven et al., 2018).

q-PCR

cDNA, primer, SYBR, and water were mixed in a qPCR plate. The qPCR reaction was performed using a QuantStudio 3 Real-Time PCR System (Thermo Fisher). In these qPCR

514 reactions, the melting temperature was 95℃ and the annealing/elongation temperature was
515 60℃. Primers used for the qPCR reactions are listed in Supplemental Table 1.

516 *RNA-FISH and Immunofluorescence (IF)*

517 At sacrificing, pieces of liver were placed within Tissue-Tek OCT (Optimal Cutting
518 Temperature) Compound and frozen with dry ice. These frozen blocks were sectioned at 10 μm
519 with a Leica CM3050 S cryostat at the Carl R. Woese Institute for Genomic Biology (UIUC).

520 RNA-FISH/IF was performed on these cryosections. Sections were washed in 1X PBS,
521 then fixed with 10% NBF. Slides were washed with 1X PBS, permeabilized with 0.5% Triton-X in
522 1X PBS, washed with 1X SSC, and then washed with 30% Formamide in 2X SSC. FISH probe
523 was then applied (the solution contained 2 μg/mL BSA, 66 μg/mL yeast tRNA, and 1 ng/μL Cy5-
524 $(CAG)_{10}$ (Integrated DNA Technologies) dissolved in 30% formamide in 2X SSC). After
525 incubation at 37℃ for two hours, sections were washed with 30% formamide in 2X SSC (for 30
526 minutes) and washed twice with 1X SSC. The slides were again fixed with 10% NBF, washed
527 with 1X TBS, and re-permeabilized with 0.5% Triton-X in PBS. Slides were washed in 1X TBS
528 before being blocked in 10% normal goat serum with 1% BSA in 1X TBS for two hours (at room
529 temperature). After blocking, the slides were drained with a vacuum trap and incubated in 1:500
530 primary antibody in 1X TBS with 1% BSA, at 4℃ overnight.

531 The next day, the slides were washed in 1X TBS with 0.05% Triton-X, then washed in
532 1X TBS. Then, they were incubated in 1:500 secondary antibody in 1X TBS for 1 hour at room
533 temperature. Slides were washed with TBS with 0.05% Triton-X, washed with 1X PBS, stained
534 with NucBlue (Invitrogen) in 1X PBS for 20 minutes, and washed with 1X PBS. Slides
535 were imaged on a Zeiss LSM 710 microscope at the Carl R. Woese Institute for Genomic
536 biology at UIUC. A list of antibodies used is provided in Supplemental Table X.

537 *RT-PCR Splice Assays*

538 Target events were amplified via PCR using the primers listed in Supplemental Table X.
539 The PCR cycle had a melting temperature of 95℃, an annealing temperature of 55℃, and an

elongation temperature of 72℃. The PCR product was resolved down a 5.5% PAGE gel, stained with ethidium bromide, and imaged using a Bio-Rad Gel Doc machine.

To quantify the percent splicing change, Bio-Rad Image Lab Software (version 6.0.1) was used to measure the intensity of the bands appearing of the gel. Splicing change is reported as Percent Spliced In, a ratio of the intensity of the upper band (containing the alternatively spliced exon) to the combined intensity of the upper and lower bands (the lower band does not contain the alternatively spliced exon).

Histology: Hematoxylin and Eosin

To perform Hematoxylin and Eosin staining, paraffin embedded tissues were sectioned into 5 µm thick sections, and then deparaffinized with three xylene washes. The slides were rehydrated in ethanol solutions of decreasing concentration (100%, 95%, 80%, and 50%) before being placed in water. The slides were stained with Hematoxylin 7211 for 1.5 to 2 minutes and washed in water. Slides were blued in a 2% sodium bicarbonate, 0.2% magnesium sulfate bluing solution before being washed in water again. After being placed in an ethanol solution, the slides were stained with eosin for 15-20 seconds, washed with ethanol, and dehydrated with xylene. They were finally mounted/cover slipped with Permount.

All slides were imaged by on a Hamamatsu Nanozoomer at the Carl R. Woese Institute for Genomic Biology at UIUC.

Histology: Oil Red O. Staining

Oil Red O. stain was performed on cryosections (reference “RNA-FISH and Immunofluorescence (IF)” for details on the preparation of cryosections). The cryosections were first fixed in 10% NBF, then hydrated in 1X PBS. After placing the slides in 60% isopropanol, the slides were stained in fresh Oil Red O. solution (consisting of Oil Red O. dye dissolved in 60% isopropanol). The slides were then washed with 60% isopropanol, counterstained briefly in Hematoxylin 7211 and washed with tap water. The slides were then mounted with CC mount.

The slides were imaged on a Hamamatsu Nanozoomer at the Carl R. Woese Institute for Genomic Biology at UIUC.

To quantitatively measure the accumulation of lipids, Oil Red O. Images at 10X zoom were collected and then analyzed using a pipeline on Cell Profiler (Kamentsky et al., 2011; Mcquin et al., 2018).

Lipid Extraction and Analysis

Twenty to fifty milligrams of liver tissue were weighed into locking cap 1.5 mL Eppendorf tubes. To this was added 600 µL chilled 3:2 hexanes/isopropanol solution and 6-10 NextAdvanced zirconium oxide 1mm beads. The tubes were homogenized on a bullet blender for 30 seconds, and then allowed to rest on ice for 2 min. This homogenization process was repeated a total of 5 times before samples were spun down at *3000 x g* for 10 min in temperatures at 4℃. The liquid phase was then collected into a second Eppendorf tube and set aside. An additional 600 µL chilled 3:2 hexanes/isopropanol solution was then used to break up the pellet, and samples were rested on ice for 15 min with periodic vortexing. Again, samples centrifuged at *3000 x g* for 10 min, and the liquid phase was then combined with the liquid set aside previously. Samples were then allowed to dry in open air over night.

Samples were then diluted in 200 µL of 1x PBS with 2% Triton X-100. Samples were vortexed and allowed to dissolve at 4C; further dilution would occur if necessary. Once samples had been dissolved, they were analyzed using an Infinity triglycerides colorimetric kit.

Serum Alanine Aminotransferase (ALT) and Aspartate Aminotransferase (AST) Testing

Whole blood from mice was collected via retro-orbital puncture in Capiject gel/clot activator tubes, centrifuged for 3 min at 3000 × *g*, and then stored at −80 °C till further analysis. ALT and AST analysis is performed using commercial Thermo Scientific serum chemistry kits

Zoxazolamine Recovery Testing

Zoxazolamine (Zox) solution was prepared the day prior to experimentation by dissolving enough Zox in DMSO such that the final concentration of Zox was 15 ug/µL in a 95% Corn-Oil,

591 5% DMSO solution. Mice were then fasted for 18-22 hours prior to 120 mg/kg Zox injections;
592 Zox solutions were homogenized vigorously between injections to ensure a homogenous
593 solution.
594 Once treated with Zox, mice could roam freely until motor function was lost, at which point mice
595 would be placed in the supine position on an insulating blanket. Time would then be measured
596 until the mice were able to regain muscle control. Time counting ceased when the mouse could
597 successfully self-right three times(Fujii et al., 1968).
598 *APAP Insult Testing*
599 Acetaminophen (APAP) solutions were prepared immediately before use. Twenty mg of
600 APAP would be dissolved in one mL of sterile 1x PBS. This solution would then be heated at
601 55C for 15 min with periodic vortexing. Once the 15 min incubation was complete, the APAP
602 solution would be kept at 40C for the duration of the injection process, and vigorous mixing
603 would occur between injections.
604 Mice for APAP testing were fasted overnight (18-22 hours) and then injected with either
605 350 mg/kg. Mice would then be observed for 8 hours, at which point the surviving mice were
606 returned to the mouse facilities. The following day, mice would be harvested for serum and liver
607 samples 24hrs post APAP injection(McGill et al., 2012; Mossanen & Tacke, 2015).
608 *Statistical Analysis*
609 All quantitative experiments have at least three independent biological repeats. The
610 results were expressed with mean and standard deviation, unless mentioned otherwise.
611 Differences between groups were examined for statistical significance using or one-way
612 analysis of variance (ANOVA) for more than two groups using the GraphPad Prism 6
613 Software. In all figures, significance was set as $p \leq 0.05$, "*" indicates $p < 0.05$, "**" indicates $p <$
614 0.01, "***" indicates $p < 0.001$, and "****" indicates $p < 0.0001$.
615

References

Achiron, A., Barak, Y., Magal, N., Shohat, M., Cohen, M., Barar, R., & Gadoth, N. (1998). Abnormal liver test results in myotonic dystrophy. *Journal of Clinical Gastroenterology*, *26*(4), 292–295. https://doi.org/10.1097/00004836-199806000-00016

Anders, S., Pyl, P. T., & Huber, W. (2015). HTSeq--a Python framework to work with high-throughput sequencing data. *Bioinformatics*, *31*(2), 166–169. https://doi.org/10.1093/bioinformatics/btu638

Ashizawa, T., Gagnon, C., Groh, W. J., Gutmann, L., Johnson, N. E., Meola, G., Moxley, R., Pandya, S., Rogers, M. T., Simpson, E., Angeard, N., Bassez, G., Berggren, K. N., Bhakta, D., Bozzali, M., Broderick, A., Byrne, J. L. B., Campbell, C., Cup, E., … Winblad, S. (2018). Consensus-based care recommendations for adults with myotonic dystrophy type 1. *Neurology: Clinical Practice*, *8*(6), 507–520. https://doi.org/10.1212/CPJ.0000000000000531

Bangru, S., Arif, W., Seimetz, J., Bhate, A., Chen, J., Rashan, E. H., Carstens, R. P., Anakk, S., & Kalsotra, A. (2018). Alternative splicing rewires Hippo signaling pathway in hepatocytes to promote liver regeneration. *Nature Structural & Molecular Biology*, *25*(10), 928–939. https://doi.org/10.1038/s41594-018-0129-2

Benoit-Pilven, C., Marchet, C., Chautard, E., Lima, L., Lambert, M.-P., Sacomoto, G., Rey, A., Cologne, A., Terrone, S., Dulaurier, L., Claude, J.-B., Bourgeois, C. F., Auboeuf, D., & Lacroix, V. (2018). Complementarity of assembly-first and mapping-first approaches for alternative splicing annotation and differential analysis from RNAseq data. *Scientific Reports*, *8*(1). https://doi.org/10.1038/s41598-018-21770-7

Bhardwaj, R. R., & Duchini, A. (2010). Non-alcoholic steatohepatitis in myotonic dystrophy: DMPK gene mutation, insulin resistance and development of steatohepatitis. *Case Reports in Gastroenterology*, *4*(1), 100–103. https://doi.org/10.1159/000292093

Bhate, A., Parker, D. J., Bebee, T. W., Ahn, J., Arif, W., Rashan, E. H., Chorghade, S., Chau, A., Lee, J.-H., Anakk, S., Carstens, R. P., Xiao, X., & Kalsotra, A. (2015). *ESRP2 controls an adult splicing programme in hepatocytes to support postnatal liver maturation*. *6*, 8768. https://doi.org/10.1038/ncomms9768

Bonnot, T., Gillard, M. B., & Nagel, D. H. (2019). A Simple Protocol for Informative Visualization of Enriched Gene Ontology Terms. *Bio-Protocol*, *9*(22), e3429. https://doi.org/10.21769/BioProtoc.3429

Brook, J. D., Mccurrach, M. E., Harley, H. G., Buckler, A. J., Church, D., Aburatani, H., Hunter, K., Stanton, V. P., Thirion, J.-P., Hudson, T., Sohn, R., Zemelman, B., Snell, R. G., Rundle, S. A., Crow, S., Davies, J., Shelbourne, P., Buxton, J., Jones, C., … Housman, D. E. (1992). *Molecular basis of myotonic dystrophy: Expansion of a trinucleotide (CTG) repeat at the 3' end of a transcript encoding a protein kinase family member*. *68*(4), 799–808. https://doi.org/10.1016/0092-8674(92)90154-5

656 Brunner, H. G., Nillesen, W., Van Oost, B. A., Jansen, G., Wieringa, B., Ropers, H. H.,
657 & Smeets, H. J. (1992). Presymptomatic diagnosis of myotonic dystrophy. *Journal*
658 *of Medical Genetics*, *29*(11), 780–784. https://doi.org/10.1136/jmg.29.11.780

659 Campbell, N., Brandom, B., Day, J. W., & Moxley, R. (2010). *Practical Suggestions for*
660 *the Anesthetic Management of a Myotonic Dystrophy Patient FOREWORD :*
661 *1*(May), 1–6.

662 Chau, A., & Kalsotra, A. (2015). Developmental insights into the pathology of and
663 therapeutic strategies for DM1: Back to the basics. *Developmental Dynamics*,
664 *244*(3), 377–390. https://doi.org/10.1002/dvdy.24240

665 Day, J. W., & Ranum, L. P. W. (2005). Genetics and molecular pathogenesis of the
666 myotonic dystrophies. *Current Neurology and Neuroscience Reports*, *5*(1), 55–60.
667 https://doi.org/10.1007/s11910-005-0024-1

668 Elmgren, A., Lelliott, C. J., Oscarsson, J., Bohlooly-Y, M., Törnell, J., Bjursell, M.,
669 Egecioglu, E., & Gerdin, A.-K. (2007). Acutely reduced locomotor activity is a major
670 contributor to Western diet-induced obesity in mice. *American Journal of*
671 *Physiology-Endocrinology and Metabolism*, *294*(2), E251–E260.
672 https://doi.org/10.1152/ajpendo.00401.2007

673 Escolà-Gil, J. C., Llaverias, G., Julve, J., Jauhiainen, M., Méndez-González, J., &
674 Blanco-Vaca, F. (2011). The cholesterol content of western diets plays a major role
675 in the paradoxical increase in high-density lipoprotein cholesterol and upregulates
676 the macrophage reverse cholesterol transport pathway. *Arteriosclerosis,*
677 *Thrombosis, and Vascular Biology*, *31*(11), 2493–2499.
678 https://doi.org/10.1161/ATVBAHA.111.236075

679 Fujii, K., Jaffe, H., & Epstein, S. S. (1968). Factors influencing the hexobarbital sleeping
680 time and zoxazolamine paralysis time in mice. *Toxicology and Applied*
681 *Pharmacology*, *13*(3), 431–438. https://doi.org/10.1016/0041-008x(68)90119-1

682 Groh, W. J., Groh, M. R., Saha, C., Kincaid, J. C., Simmons, Z., Ciafaloni, E.,
683 Pourmand, R., Otten, R. F., Bhakta, D., Nair, G. V, Marashdeh, M. M., Zipes, D. P.,
684 & Pascuzzi, R. M. (2008). Electrocardiographic Abnormalities and Sudden Death in
685 Myotonic Dystrophy Type 1. *New England Journal of Medicine*, *358*(25), 2688–
686 2697. https://doi.org/10.1056/nejmoa062800

687 Ha, K. C. H., Blencowe, B. J., & Morris, Q. (2018). QAPA: a new method for the
688 systematic analysis of alternative polyadenylation from RNA-seq data. *Genome*
689 *Biology*, *19*(1). https://doi.org/10.1186/s13059-018-1414-4

690 Harper, P. S. (2003). *Myotonic Dystrophy* (3rd ed.). W.B. Saunders.

691 Heatwole, C., Bode, R., Johnson, N., Quinn, C., Martens, W., McDermott, M. P.,
692 Rothrock, N., Thornton, C., Vickrey, B., Victorson, D., & Moxley, R. (2012). Patient-
693 reported impact of symptoms in myotonic dystrophy type 1 (PRISM-1). *Neurology*,
694 *79*(4), 348–357. https://doi.org/10.1212/WNL.0b013e318260cbe6

695 Ho, T. H., Charlet-B, N., Poulos, M. G., Singh, G., Swanson, M. S., & Cooper, T. A.

(2004). Muscleblind proteins regulate alternative splicing. *EMBO Journal*, *23*(15), 3103–3112. https://doi.org/10.1038/sj.emboj.7600300

Huang, D. W., Sherman, B. T., & Lempicki, R. A. (2009). Systematic and integrative analysis of large gene lists using DAVID bioinformatics resources. *Nature Protocols*, *4*(1), 44–57. https://doi.org/10.1038/nprot.2008.211

Huang, D. W., Sherman, B. T., Tan, Q., Kir, J., Liu, D., Bryant, D., Guo, Y., Stephens, R., Baseler, M. W., Lane, H. C., & Lempicki, R. A. (2007). DAVID Bioinformatics Resources: expanded annotation database and novel algorithms to better extract biology from large gene lists. *Nucleic Acids Research*, *35*(suppl_2), W169–W175. https://doi.org/10.1093/nar/gkm415

Jiang, H., Mankodi, A., Swanson, M. S., Moxley, R. T., & Thornton, C. A. (2004). Myotonic dystrophy type 1 is associated with nuclear foci of mutant RNA, sequestration of muscleblind proteins and deregulated alternative splicing in neurons. *Human Molecular Genetics*, *13*(24), 3079–3088. https://doi.org/10.1093/hmg/ddh327

John Herbick, C. J. (2013). Hepatic Glycogenosis in a Patient with Type 1 Myotonic Dystrophy. *Journal of Liver: Disease & Transplantation*, *02*(02), 2012–2014. https://doi.org/10.4172/2325-9612.1000110

Kamentsky, L., Jones, T. R., Fraser, A., Bray, M.-A., Logan, D. J., Madden, K. L., Ljosa, V., Rueden, C., Eliceiri, K. W., & Carpenter, A. E. (2011). Improved structure, function and compatibility for CellProfiler: modular high-throughput image analysis software. *Bioinformatics*, *27*(8), 1179–1180. https://doi.org/10.1093/bioinformatics/btr095

Kanadia, R. N. (2003). A Muscleblind Knockout Model for Myotonic Dystrophy. *Science*, *302*(5652), 1978–1980. https://doi.org/10.1126/science.1088583

Kent, W. J., Sugnet, C. W., Furey, T. S., Roskin, K. M., Pringle, T. H., Zahler, A. M., & Haussler, A. D. (2002). The Human Genome Browser at UCSC. *Genome Research*, *12*(6), 996–1006. https://doi.org/10.1101/gr.229102

Lee, J., Bai, Y., Chembazhi, U. V, Peng, S., Yum, K., Luu, L. M., Hagler, L. D., Serrano, J. F., Chan, H. Y. E., Kalsotra, A., & Zimmerman, S. C. (2019). Intrinsically cell-penetrating multivalent and multitargeting ligands for myotonic dystrophy type 1. *Proceedings of the National Academy of Sciences*, *116*(18), 8709–8714. https://doi.org/10.1073/pnas.1820827116

Lee, J. E., & Cooper, T. A. (2009). Pathogenic mechanisms of myotonic dystrophy. *Biochemical Society Transactions*, *37*(6), 1281–1286. https://doi.org/10.1042/bst0371281

Li, W.-C., Ralphs, K. L., & Tosh, D. (2010). Isolation and Culture of Adult Mouse Hepatocytes. In *Methods in Molecular Biology* (pp. 185–196). Humana Press. https://doi.org/10.1007/978-1-59745-019-5_13

Lin, X., Miller, J. W., Mankodi, A., Kanadia, R. N., Yuan, Y., Moxley, R. T., Swanson, M.

S., & Thornton, C. A. (2006). Failure of MBNL1-dependent post-natal splicing transitions in myotonic dystrophy. *Human Molecular Genetics*, *15*(13), 2087–2097. https://doi.org/10.1093/hmg/ddl132

Love, M. I., Huber, W., & Anders, S. (2014). Moderated estimation of fold change and dispersion for RNA-seq data with DESeq2. *Genome Biology*, *15*(12). https://doi.org/10.1186/s13059-014-0550-8

Machuca-Tzili, L., Brook, D., & Hilton-Jones, D. (2005). Clinical and molecular aspects of the myotonic dystrophies: A review. *Muscle & Nerve*, *32*(1), 1–18. https://doi.org/10.1002/mus.20301

Mankodi, A. (2000). *Myotonic Dystrophy in Transgenic Mice Expressing an Expanded CUG Repeat*. *289*(5485), 1769–1772. https://doi.org/10.1126/science.289.5485.1769

Mathieu, J., Allard, P., Gobeil, G., Girard, M., De Braekeleer, M., & Bégin, P. (1997). Anesthetic and surgical complications in 219 cases of myotonic dystrophy. *Neurology*, *49*(6), 1646 LP – 1650. https://doi.org/10.1212/WNL.49.6.1646

McGill, M. R., Williams, C. D., Xie, Y., Ramachandran, A., & Jaeschke, H. (2012). Acetaminophen-induced liver injury in rats and mice: Comparison of protein adducts, mitochondrial dysfunction, and oxidative stress in the mechanism of toxicity. *Toxicology and Applied Pharmacology*. https://doi.org/10.1016/j.taap.2012.08.015

Mcquin, C., Goodman, A., Chernyshev, V., Kamentsky, L., Cimini, B. A., Karhohs, K. W., Doan, M., Ding, L., Rafelski, S. M., Thirstrup, D., Wiegraebe, W., Singh, S., Becker, T., Caicedo, J. C., & Carpenter, A. E. (2018). CellProfiler 3.0: Next-generation image processing for biology. *PLOS Biology*, *16*(7), e2005970. https://doi.org/10.1371/journal.pbio.2005970

Miller, J. W. (2002). Recruitment of human muscleblind proteins to (CUG)n expansions associated with myotonic dystrophy. *The EMBO Journal*, *19*(17), 4439–4448. https://doi.org/10.1093/emboj/19.17.4439

Morriss, G. R., Rajapakshe, K., Huang, S., Coarfa, C., & Cooper, T. A. (2018). Mechanisms of skeletal muscle wasting in a mouse model for myotonic dystrophy type 1. *Human Molecular Genetics*, *27*(16), 2789–2804. https://doi.org/10.1093/hmg/ddy192

Mossanen, jc, & Tacke, f. (2015). Acetaminophen-induced acute liver injury in mice. *Laboratory Animals*. https://doi.org/10.1177/0023677215570992

Park, J. W., Jung, S., Rouchka, E. C., Tseng, Y.-T., & Xing, Y. (2016). rMAPS: RNA map analysis and plotting server for alternative exon regulation. *Nucleic Acids Research*, *44*(W1), W333–W338. https://doi.org/10.1093/nar/gkw410

Patro, R., Duggal, G., Love, M. I., Irizarry, R. A., & Kingsford, C. (2017). Salmon provides fast and bias-aware quantification of transcript expression. *Nature Methods*, *14*(4), 417–419. https://doi.org/10.1038/nmeth.4197

776 Philips, A. V, Timchenko, L. T., & Cooper, T. A. (1998). Disruption of splicing regulated
777 by a CUG-binding protein in myotonic dystrophy. *Science (New York, N.Y.)*,
778 *280*(5364), 737–741. https://doi.org/10.1126/science.280.5364.737

779 Savkur, R. S., Philips, A. V, & Cooper, T. A. (2001). Aberrant regulation of insulin
780 receptor alternative splicing is associated with insulin resistance in myotonic
781 dystrophy. *Nature Genetics*, *29*(1), 40–47. https://doi.org/10.1038/ng704

782 Scotti, M. M., & Swanson, M. S. (2015). *RNA mis-splicing in disease*. *17*(1), 19–32.
783 https://doi.org/10.1038/nrg.2015.3

784 Scotti, M. M., & Swanson, M. S. (2016). RNA mis-splicing in disease. *Nature Reviews*
785 *Genetics*, *17*(1), 19–32. https://doi.org/10.1038/nrg.2015.3

786 Shen, S., Park, J. W., Lu, Z., Lin, L., Henry, M. D., Wu, Y. N., Zhou, Q., & Xing, Y.
787 (2014). rMATS: robust and flexible detection of differential alternative splicing from
788 replicate RNA-Seq data. *Proceedings of the National Academy of Sciences of the*
789 *United States of America*, *111*(51), E5593-601.
790 https://doi.org/10.1073/pnas.1419161111

791 Shieh, K., Gilchrist, J. M., & Promrat, K. (2010). Frequency and predictors of
792 nonalcoholic fatty liver disease in myotonic dystrophy. *Muscle and Nerve*, *41*(2),
793 197–201. https://doi.org/10.1002/mus.21484

794 Sobczak, K., Thornton, C. A., Finn, D. J., Manchanda, M., Mohan, A., Goodwin, M.,
795 Charizanis, K., Zhang, C., Batra, R., Li, M., & Swanson, M. S. (2014). Loss of
796 MBNL Leads to Disruption of Developmentally Regulated Alternative
797 Polyadenylation in RNA-Mediated Disease. *Molecular Cell*, *56*(2), 311–322.
798 https://doi.org/10.1016/j.molcel.2014.08.027

799 Supek, F., Bošnjak, M., Škunca, N., & Šmuc, T. (2011). REVIGO Summarizes and
800 Visualizes Long Lists of Gene Ontology Terms. *PLoS ONE*, *6*(7), e21800.
801 https://doi.org/10.1371/journal.pone.0021800

802 Trapnell, C., Roberts, A., Goff, L., Pertea, G., Kim, D., Kelley, D. R., Pimentel, H.,
803 Salzberg, S. L., Rinn, J. L., & Pachter, L. (2012). Differential gene and transcript
804 expression analysis of RNA-seq experiments with TopHat and Cufflinks. *Nature*
805 *Protocols*, *7*(3), 562–578. https://doi.org/10.1038/nprot.2012.016

806 Turner, C, & Hilton-Jones, D. (2010). *The myotonic dystrophies: diagnosis and*
807 *management*. *81*(4), 358–367. https://doi.org/10.1136/jnnp.2008.158261

808 Turner, Chris, & Hilton-Jones, D. (2010). The myotonic dystrophies: Diagnosis and
809 management. *Journal of Neurology, Neurosurgery and Psychiatry*, *81*(4), 358–367.
810 https://doi.org/10.1136/jnnp.2008.158261

811 Veyckemans, F., & Scholtes, J. L. (2013). Myotonic DYSTROPHIES type 1 and 2:
812 Anesthetic care. *Paediatric Anaesthesia*, *23*(9), 794–803.
813 https://doi.org/10.1111/pan.12120

814 Wang, E. T., Cody, N. A. L., Jog, S., Biancolella, M., Wang, T. T., Treacy, D. J., Luo, S.,
815 Schroth, G. P., Housman, D. E., Reddy, S., Lécuyer, E., & Burge, C. B. (2012).

816 Transcriptome-wide regulation of pre-mRNA splicing and mRNA localization by
817 muscleblind proteins. *Cell*, *150*(4), 710–724.
818 https://doi.org/10.1016/j.cell.2012.06.041

819 Wang, E. T., Treacy, D., Eichinger, K., Struck, A., Estabrook, J., Olafson, H., Wang, T.
820 T., Bhatt, K., Westbrook, T., Sedehizadeh, S., Ward, A., Day, J., Brook, D.,
821 Berglund, J. A., Cooper, T., Housman, D., Thornton, C., & Burge, C. (2019).
822 Transcriptome alterations in myotonic dystrophy skeletal muscle and heart. *Human*
823 *Molecular Genetics*, *28*(8), 1312–1321. https://doi.org/10.1093/hmg/ddy432

824 Wheeler, T. M., & Thornton, C. A. (2007). Myotonic dystrophy: RNA-mediated muscle
825 disease. *Current Opinion in Neurology*, *20*(5), 572–576.
826 https://doi.org/10.1097/WCO.0b013e3282ef6064

827 Xu, K., Deng, X. Y., Yue, Y., Guo, Z. M., Huang, B., Hong, X., Xiao, D., & Chen, X. G.
828 (2005). Generation of the regulatory protein rtTA transgenic mice. *World Journal of*
829 *Gastroenterology*, *11*(19), 2885–2891. https://doi.org/10.3748/wjg.v11.i19.2885

830 Yum, K., Wang, E. T., & Kalsotra, A. (2017). Myotonic dystrophy: disease repeat range,
831 penetrance, age of onset, and relationship between repeat size and phenotypes.
832 *Current Opinion in Genetics & Development*, *44*, 30–37.
833 https://doi.org/10.1016/j.gde.2017.01.007

834

Fig. 1: A murine model successfully recapitulates the molecular mechanism of DM1 within hepatocytes

A, Schematic of the bi-transgenic, hepatocyte specific, doxycycline (Dox)-inducible model used to induce expression of the toxic CUG960i RNA within the liver of mice. The toxic transcripts contain long (CUG) repeat stretches, which sequester RNA binding proteins including MBNL proteins. This model is referred to as the DM1 liver model. Feeding the mice Dox will cause the toxic RNA to be expressed within the hepatocytes of the mice. B, Experimental schematic of the Dox diet feeding protocol used induce DM1 within the livers of the subject mice. Mice are fed 2g/kg Dox supplemented rodent diet until weening on day 21. Mice are then switched to 0.1g/kg Dox supplemented diet or maintained on the 2g/kg Dox diet for a further 6 weeks. Glucose tolerance testing (GTT) occurs the week prior to sacking. C, Hybrid RNA fluorescent in-situ hybridization immuno-fluorescence (RNA FISH-IF) imaging of the toxic $(CUG)_n$ RNA (red) and Mbnl1 (green) foci within the nuclei (blue) of hepatocytes. D, Quantification of the number of CUG960i/Mbnl1 foci containing hepatocyte nuclei, as determined by RNA FISH-IF. DM1 liver mice fed 0.1g/kg Dox diet (n=7) are compared to mice either not Dox (No Dox) diet (n=5), or mice fed 0.1g/kg Dox for two months before being returned to Dox free diet for two weeks (2 week recovery) (n=7) E, Distribution of the number of CUG960i/Mbnl1 foci per hepatocyte nucleus in mice fed 0.1 g/kg Dox diet for 1 month after weening (n=7). F, Quantitative-PCR analysis of the toxic CUG960i RNA within the hepatocytes and whole liver of the DM1 liver mice and respective controls (n= 5 for the ApoE-rtTA controls, 20 for the DM1 liver mice, 9 for the DM1 mice that were not fed Dox (No-Dox), and 7 for the 2 week recovery mice).

Fig. 2: DM1 causes global transcriptomic changes within the hepatocytes

A, Reverse transcription-PCR (RT-PCR) splicing gel analysis of selected Mbnl1 targets. Bands represent either the presence or absence of the target exon, the band corresponding to (+) indicates exon inclusion and (-) indicates exon exclusion. Targets are listed above each image, with percent “spliced in” (PSI) listed below. B, Overlap of transcripts that undergo either alternative splicing, alternative poly adenylation (APA) or changes in expression upon induction of DM1 within hepatocytes. C, Volcano plot showing changes in mRNA abundance from RNA-seq (n = 3 animals per condition) D, Violin plots showing the inclusion levels of alternative splicing events that fall into the categories of mutually exclusive splicing (MXE), alternative 3’ or 5’ splicing (A3SS or A5SS), alternative cassette exon splicing (ASE), or retained intron (RI) events, as taken from the RNA-seq data. E, Comparison of exon inclusion results for 30 events. Change in PSI as determined by RT-PCR splice assays is plotted on the Y axis and change in PSI as determined by RNA Seq analysis is plotted on the x axis (n=3 animals per condition). F, Gene tracks of representative genes showing alternative exon inclusion levels across DM1 liver hepatocytes, *Mbnl1*$^{\Delta E3/\Delta E3}$ (KO) or wild type animals. G, Pie chart of genes undergoing alternative splicing when compared to control animals. Genes are divided into categories depending on if they have been shown to be regulated by DM1 alone, Mbnl1 or changing during maturation in the liver. H, Pie chart of genes undergoing alternative expression when compared to control animals. Genes are divided into categories depending on if they have been shown to be regulated by DM1 alone, Mbnl1 or changing during maturation of the liver. I, Gene ontology diagram of selected processes belonging to genes with alternative mRNA processing events in the DM1 liver model. J. Gene ontology diagram of selected processes belonging to genes undergoing differential expression in the DM1 liver model

Fig. 3: DM1 causes lipid accumulation and injury within the liver

A, Blood glucose levels of male mice, measured just prior to sacrifice after 4 hours of fasting (n= 15 for male ApoE-rtTA control mice and 16 for DM1 liver male mice). B, Glucose tolerance testing (GTT) curves of male mice, showing blood glucose levels rise and fall after IP injection of glucose. GTT was performed the week preceding harvest after a 24hr fast (n= 8 for male ApoE-rtTA control mice and 16 for DM1 liver male mice). C, Representative histological images of ApoE-rtTA control and DM1 Mice. The top two rows are representative hematoxylin and eosin (H&E) images. Instances of inflammation and necrosis are circled in the DM1 liver H&E images. The bottom row are representative Oil Red-O images. Oil Red-O (Red) stains lipid droplets; hematoxylin (blue) stains the nuclei. D, Hepatosomatic index for DM1 mice and respective ApoE-rtTA control mice (n= 16 for ApoE-rtTA mice and 32 for DM1 liver mice). E, Quantification of Oil Red O signal, relative to the signal from hematoxylin stained nuclei. Oil Red O stains lipid droplets within tissues, allowing for a relative determination of lipid accumulation when compared to number of nuclei present.

Fig. 4: DM1 increases diet induced NAFLD severity

A, A schematic of the feeding protocol used for the western diet fed mice. Mice are fed 2g/kg Dox supplemented rodent diet at birth, as before, but at weening, mice are switched to a 0.1g/kg Dox supplemented high fat, high sugar “western” diet. Mice are maintained on the western diet for 8 weeks until sacrifice. B, GTT curves. GTT was performed twice during the two weeks preceding harvest, with a 6 day resting period between each test (n= 12 for male ApoE-rtTA control mice and 9 for DM1 liver male mice, and 5 for DM1) C, Blood glucose levels of mice, measured just prior to sacrifice after 4 hours of fasting (n= 22 for male ApoE-rtTA control mice and 10 for DM1 liver male mice). D, Representative images of livers collected from ApoE-rtTA mice (left) and DM1 Liver mice (right) fed western diet. E, Representative histological images of ApoE-rtTA control and DM1 Mice. The top row are representative hematoxylin and eosin (H&E) images. Instances of inflammation and necrosis are circled in the DM1 liver H&E images. The bottom two rows are representative Oil Red-O images. Oil Red-O (Red) stains lipid droplets; hematoxylin (blue) stains the nuclei. F, Analysis of the extractable triglycerides within the livers of mice fed the basal 0.1g Dox supplemented diet and the western 0.1g Dox supplemented diet (n= 21 for ApoE-rtTA mice and 14 for DM1 liver mice). G, Hepatosomatic index for DM1 mice and respective ApoE-rtTA control mice (n= 34 for ApoE-rtTA mice and 19 for DM1 liver mice).

914 **Figure 5: DM1 liver model mice demonstrate decreased drug metabolism.**

915 A, a schematic of the zoxazolamine testing procedure utilized. Mice are given 120 mg of
916 zoxazolamine per kg of body weight via IP injection. Once mice cease movement and are
917 unable to self-right, mice are placed on their back on a heated pad, and time is measured until
918 the mice can successfully right themselves 3 times. Zoxazolamine testing was always
919 performed in batches, containing both age matched and sex matched controls along DM1 liver
920 mice. B, the average self-righting time of zoxazolamine injected mice. The time is normalized,
921 with the average control male mouse self-right time being set to 100. C, a schematic outlining
922 APAP drug metabolism within hepatocytes. D, the mortality rate of APAP insult experiments 8
923 hours post 350 mg/kg APAP injection. E, representative images of the livers of male mice which
924 survived for 24 hours post 350 mg/kg APAP injection. F, representative H&E images of livers
925 from male mice surviving 24 hours post 350 mg/kg APAP injection.

926

FIGURE 1

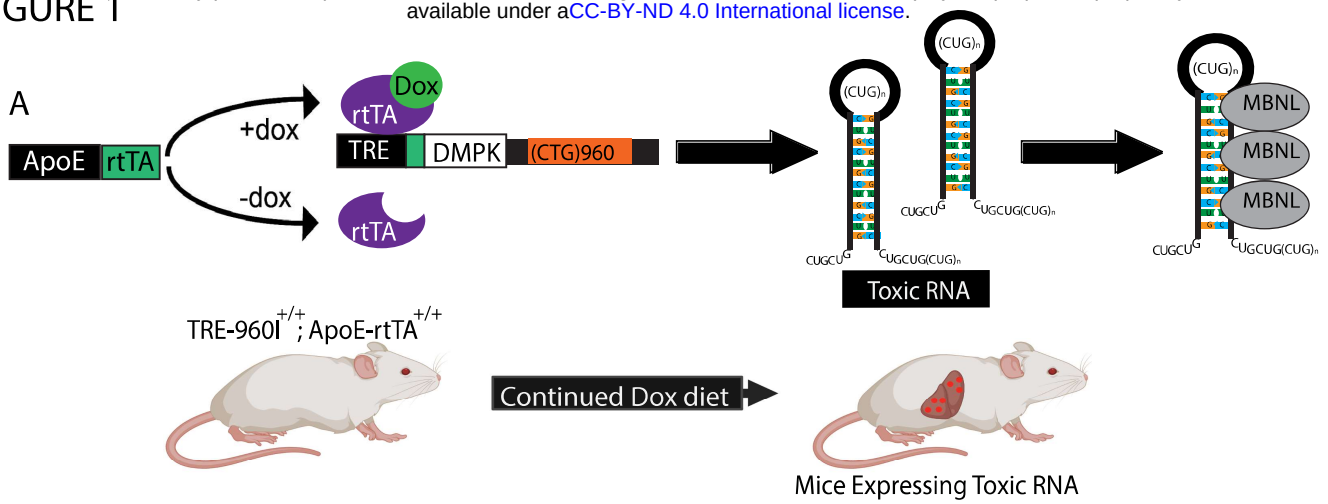

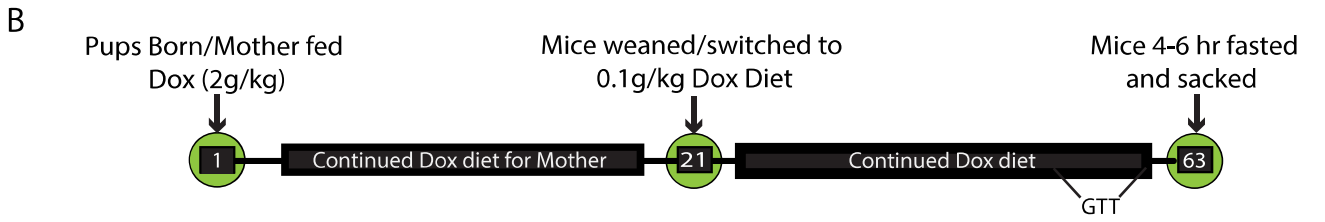

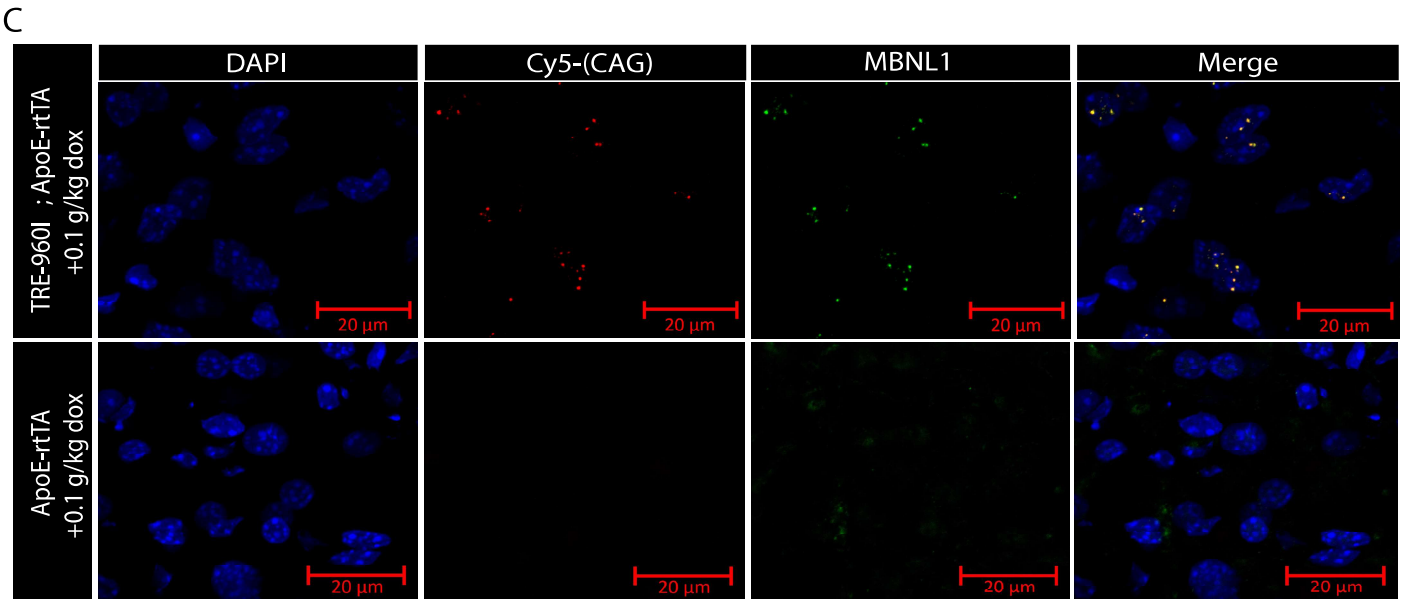

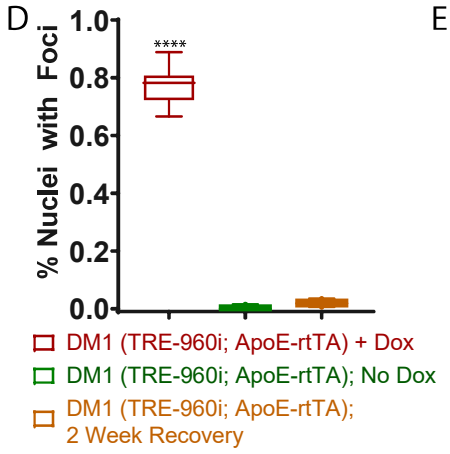

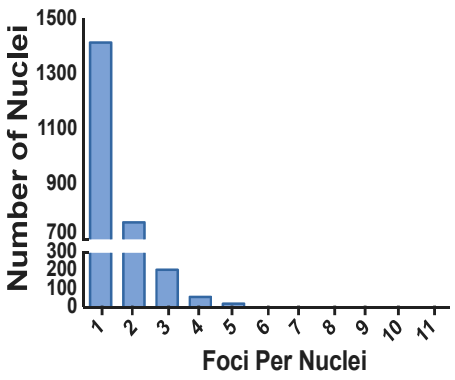

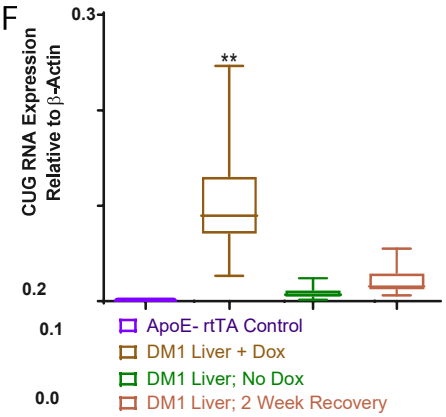

FIGURE 2

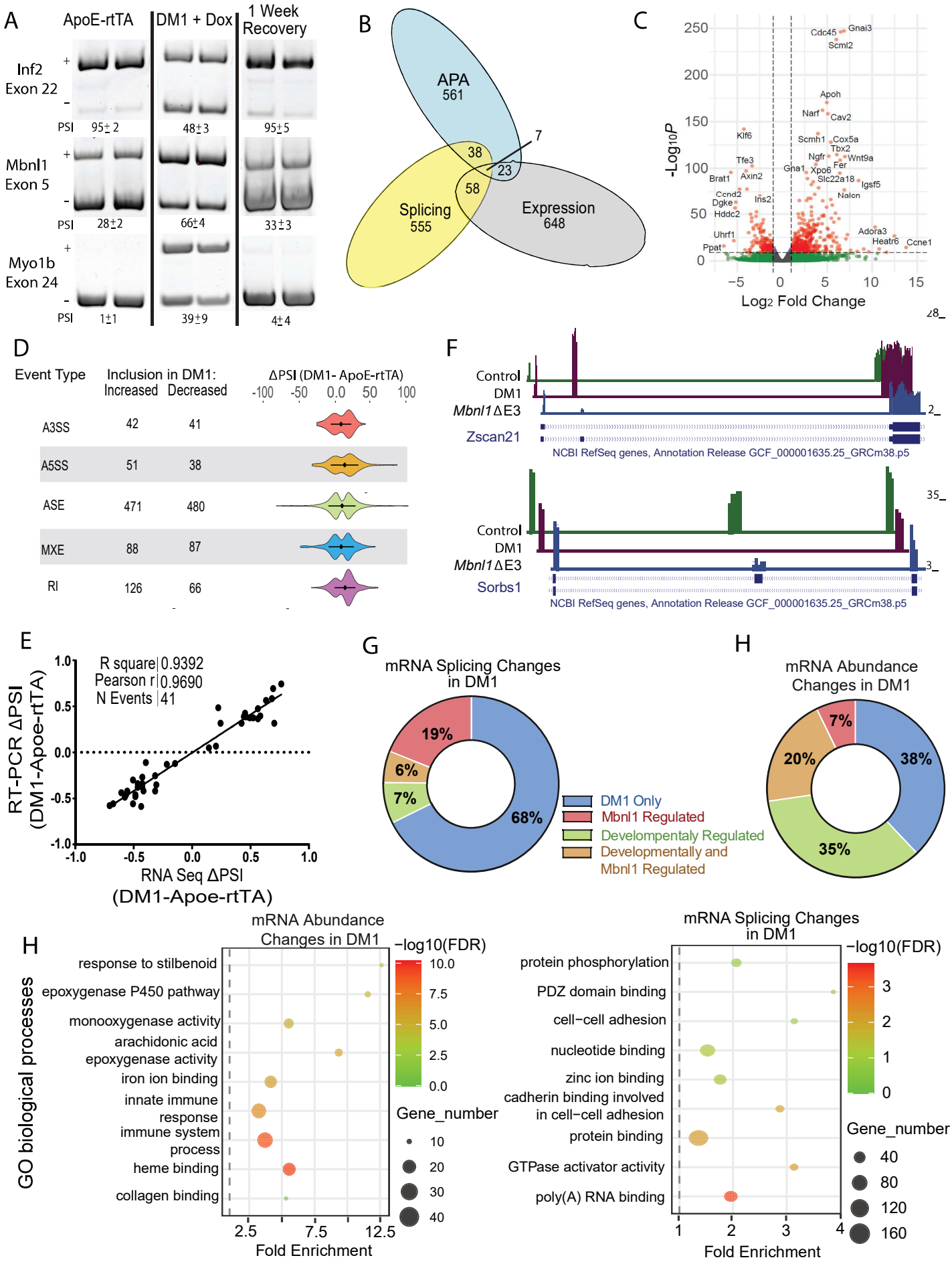

FIGURE 3

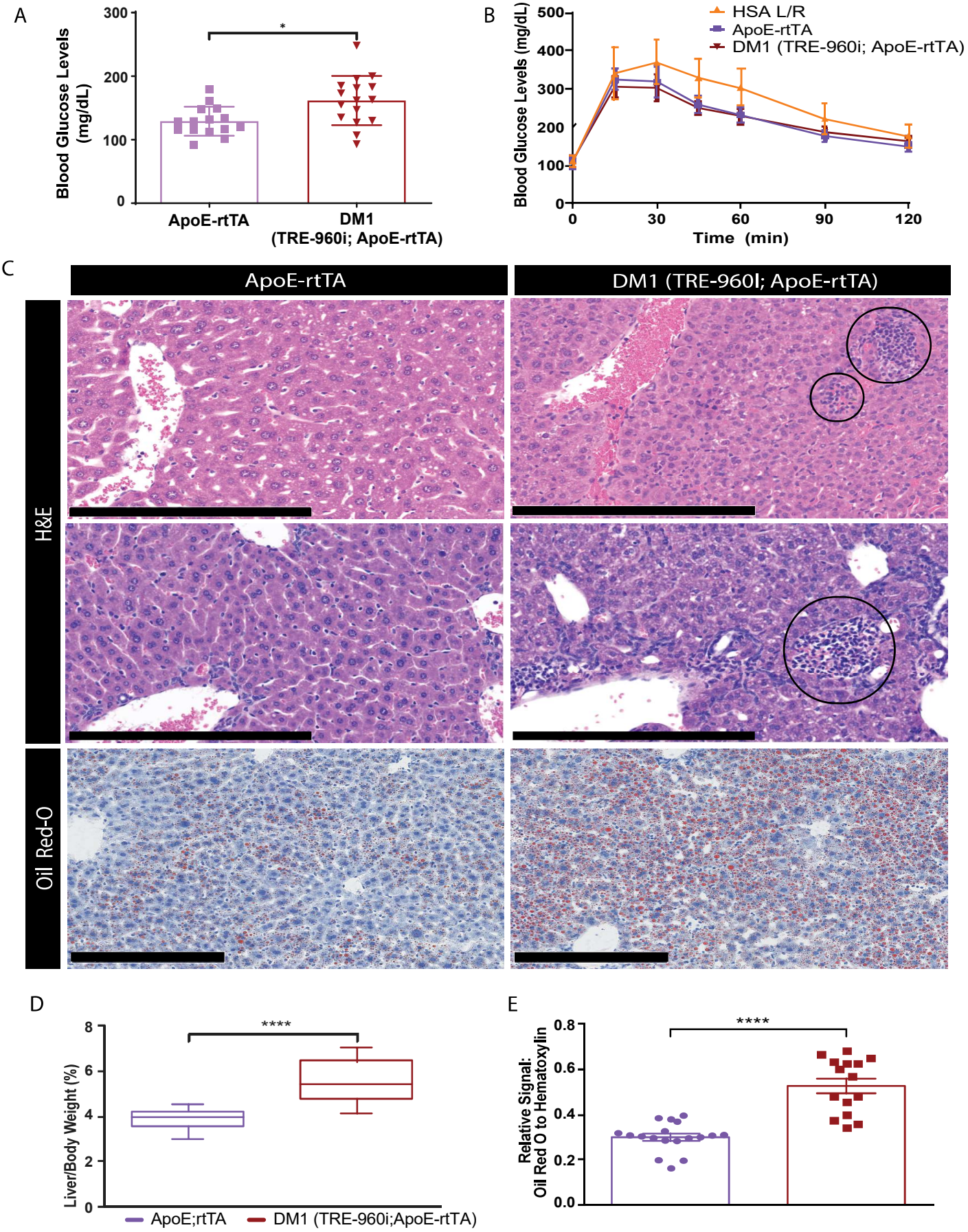

FIGURE 4

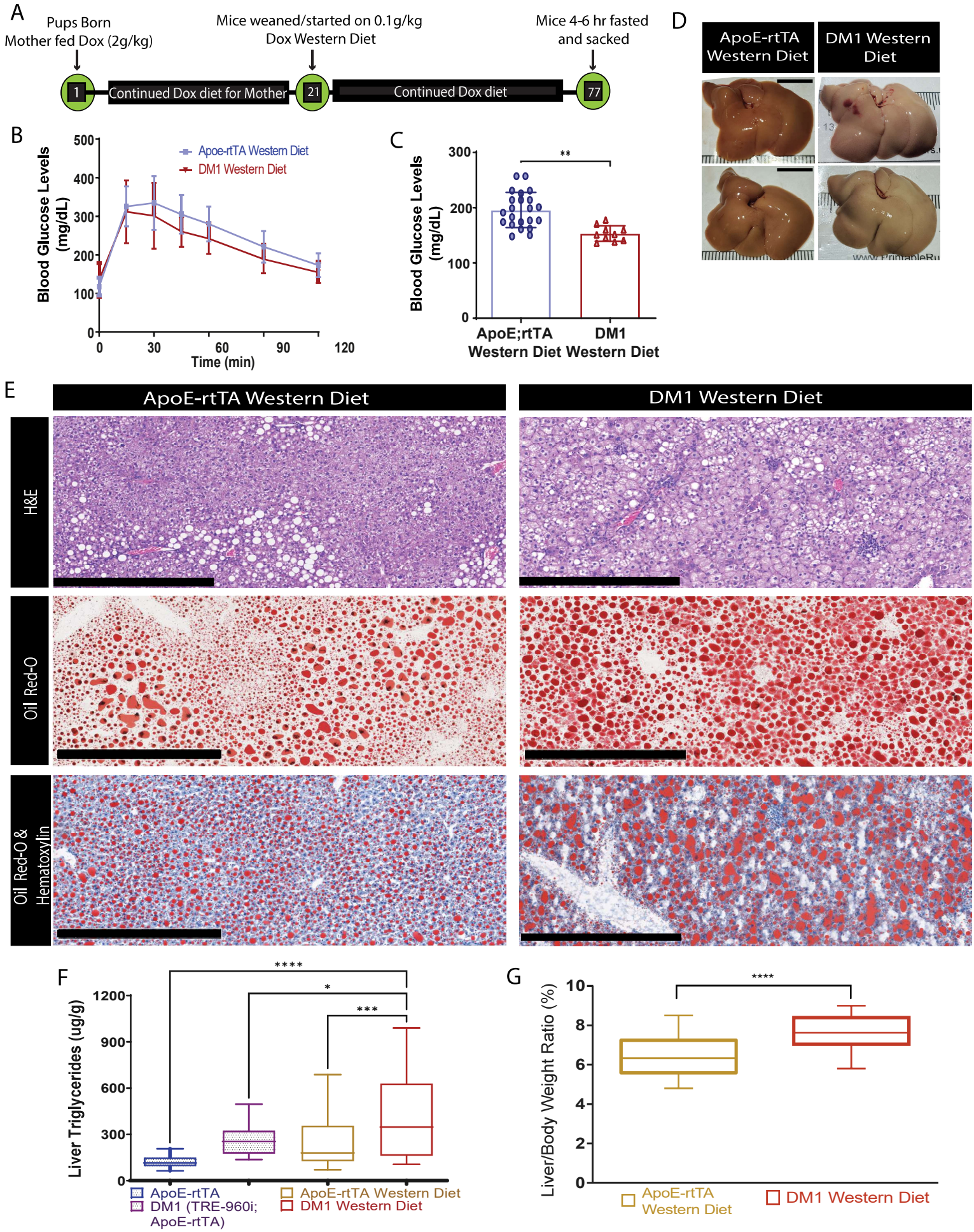

FIGURE 5

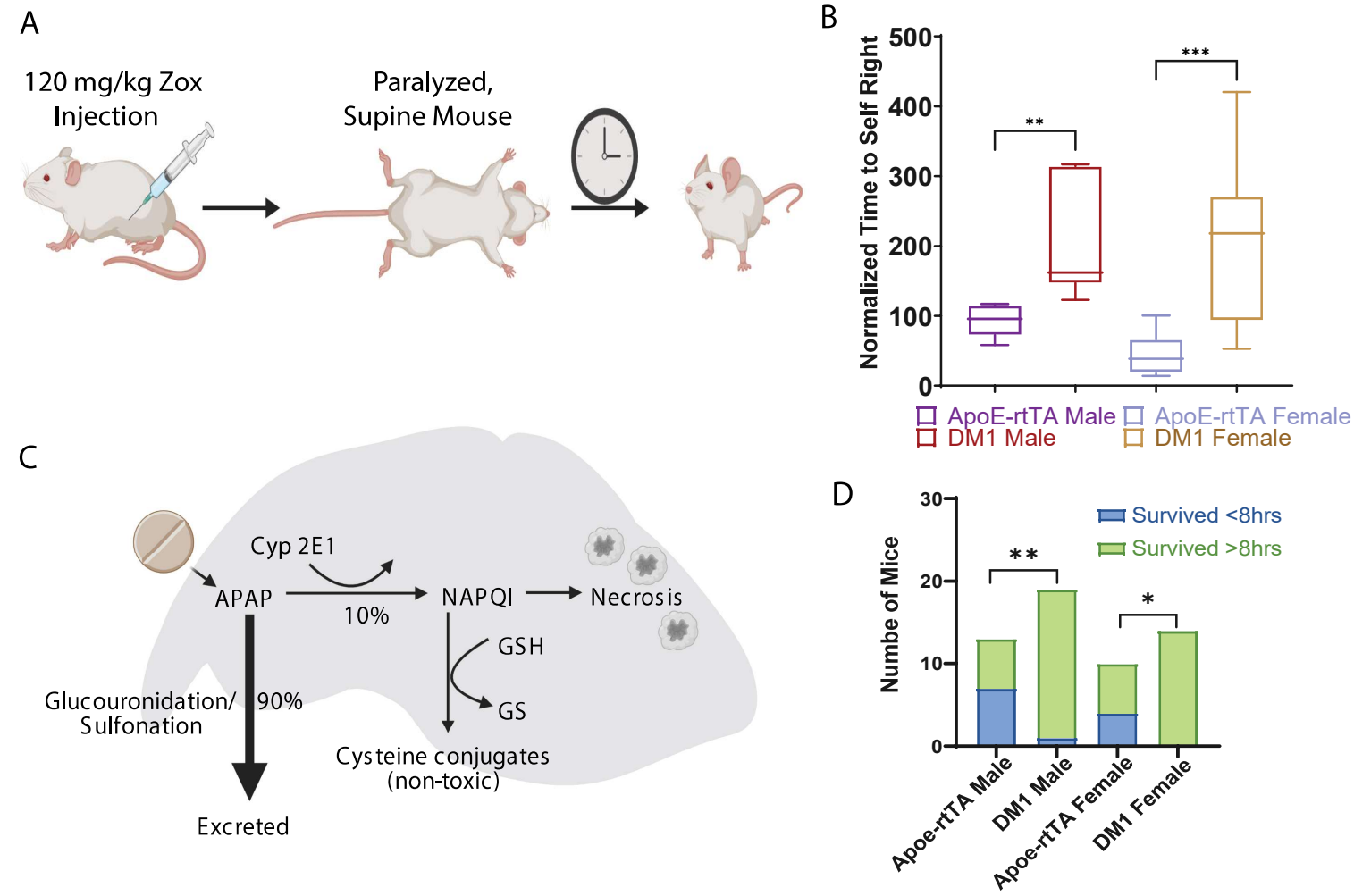

927 Table 1: Gene ontology clusters identified by DAVID Functional Annotation within DM1 induced

928 hepatocyte splicing changes

929

Cluster Name	**Example Ontologies Effected**	**Total Genes Effected**	**Enrichment Score**	**P-Value**
Zinc Finger Proteins			3.375	
	IPR001965: Zinc Finger, PHD-Type	12		6.14E-5
Kinase and Phosphorylation activity			3.166	
	GO:0000166: Nucleotide Binding	92		3.63E-5
	GO:0006468: Protein Phosphorylation	36		7.77E-5
	IPR008271: Serine/threonine-Protein Kinase	23		2.89E-4

930

931

932 Table 2: Gene ontology clusters identified by DAVID Functional Annotation within DM1 induced

933 hepatocyte transcript abundance changes

	Cluster Name	Example Ontologies Effected	Total Genes Effected	Enrichment Score	P-Value
Increasing Abundance					
	Cytochrome p450			6.286	
		GO:0020037: Heme Binding	31		3.95E-14
		IPR002401: Cytochrome P450, E-class, Group 1	18		3.29E-10
		GO:008392: Arachidonic Acid metabolism	18		1.55E-9
	Kinase and Phosphorylation activity			2.97	
		GO:0006468: Protein Phosphorylation	40		7.30E-6
		IPR001245: Serine/threonine-Protein Kinase	13		9.87E-4
	SMAD Protein Pathways	GO:060389-SMAD protein phosphorylation	5	2.89	5.64E-4

	Hormone Receptor Signaling			2.89	
		GO:0003707: Steroid Hormone Receptor Activity	9		3.69E-4
		IPR000536: Nuclear hormone receptor	8		6.03E-4
	C-type Lectin Domains	IPR016186:C-type lectin-like	13	2.48	8.69E-4
Decreasing Abundance					
	Hormone Biosynthesis	mmu00830: Retinol metabolism	7	2.48	1.69E-3
	Regulation of Development			2.41	
		mmu04950: Maturity onset diabetes of the young	6		3.91E-5
		GO:0001889~liver development	5		1.49E-3

934

935

Supplemental Figure 1: Ancillary data and liver images for 0.1g dox fed mice

A, Quantification of the number of CUG960i/Mbnl1 foci containing hepatocyte nuclei, as determined by RNA FISH-IF. Mice fed 2g/kg Dox diet (n=7) are compared to mice fed 0.1 g/kg Dox diet (n=7) B, Quantative-PCR analysis of the toxic CUG960i RNA within the hepatocytes and whole liver of the DM1 liver mice and respective controls (n=3 for the DM1 hepatocytes, 20 for the DM1 whole livers). C, Pie chart showing the percentage of alternative splicing events that fall into the categories of mutually exclusive splicing (MXE), alternative 3' or 5' splicing (A3SS or A5SS), alternative cassette exon splicing (ASE), or retained intron (RI) events, as taken from the RNA-seq data D, RT-PCR splice assay analysis of selected Mbnl1 targets. Bands represent either the presence or absence of the target exon, the band corresponding to (+) indicates exon inclusion and (-) indicates exon exclusion. Targets are listed above each image, with percent "spliced in" (PSI) listed below E, Quantification of the PSI of a variety of events changing in either *Mbnl1*$^{\Delta E3/\Delta E3}$ or DM1 liver mice or both, compared to their respective controls (n=3) F, Venn Diagram comparing mRNA differentially expressed in either the DM1 liver model or the *Mbnl1*$^{\Delta E3/\Delta E3}$ model when compared to controls. G, Venn Diagram comparing alternative mRNA processing events occurring in either the DM1 liver model or the *Mbnl1*$^{\Delta E3/\Delta E3}$ model when compared to controls. H, Western blot showing an increase of Mbnl2 protein within the *Mbnl1*$^{\Delta E3/\Delta E3}$ mice.

Supplemental Figure 2: Ancillary data and liver images for basal dox fed mice

A, Blood glucose levels of female mice, measured just prior to sacrifice after 4 hours of fasting (n= 15 for female ApoE-rtTA control mice and 13 for DM1 liver female mice). B, Glucose tolerance testing (GTT) curves of female mice, showing blood glucose levels rise and fall after IP injection of glucose. GTT was performed the week preceding harvest after a 24hr fast (n= 7 for female ApoE-rtTA control mice and 17 for DM1 liver female mice). C, Mean body masses of mice diet at sacrifice (n= 9 for male ApoE-rtTA control mice, 5 for female ApoE-rtTA control mice, 9 for DM1 male mice fed w/o Dox, 5 for DM1 liver female mice fed w/o Dox, 10 for DM1 liver male mice, and 9 for DM1 liver female mice). D, Representative histological images of HSA L/R mice livers. The top row is a representative Oil Red-O image. Oil Red-O (Red) stains lipid droplets; hematoxylin (blue) stains the nuclei. The bottom row is a representative hematoxylin and eosin (H&E) image. E, Mean body masses of mice fed western diet at sacrifice (n= 17 for male and female ApoE-rtTA control mice, 10 for DM1 liver male mice, and 9 for DM1 liver female mice).

970 **Supplemental Tables**

971 **Supplemental Table 1.** A table showing the qPCR forwards and reverse primers.

Gene	Forwards Primer	Reverse Primer
β-Actin	TTGAATGGCAAGGTGCTGGA	TACGACCAGAGGCATACA
TRE-*960i*	GGGCCGTCCGTGTTCC	GGGCGTCATGCACAAGAAAG

972

973 **Supplemental Table 2.** A table of showing the forwards and reverse primers for each splicing

974 event.

Gene	Forwards Primer	Reverse Primer
Inf2	GGATGAGGATTGAGAGGACA	GAGCACTCACTTGGCTTTGG
Mbnl1	GCTGCCCAATACCAGGTCAAC	TGGTGGGAGAAATGCTGTATGC
Synj2	TTGTCCATGAGTGCCAGAAG	GAGCTCGGTGGAGACAACTC
Sorbs1	TCAGAGTCACCAAGACATTTTATACC	ATTGGCTGGAGCAGGTCT
Myo1b	ACAAAGCGGTACCAGCAGA	TGCGTACCTTCAGTCCAAGC
Mbnl2	ATTTTCACCCTGCTGGACCAC	TTTGGTAAGGGATGAAGACCA
Git2	GATCAGGCCAGAGCCATAC	AGGGTCACAGGCAGTGTTGT

975

976

SUPPLEMENTAL FIGURE 1

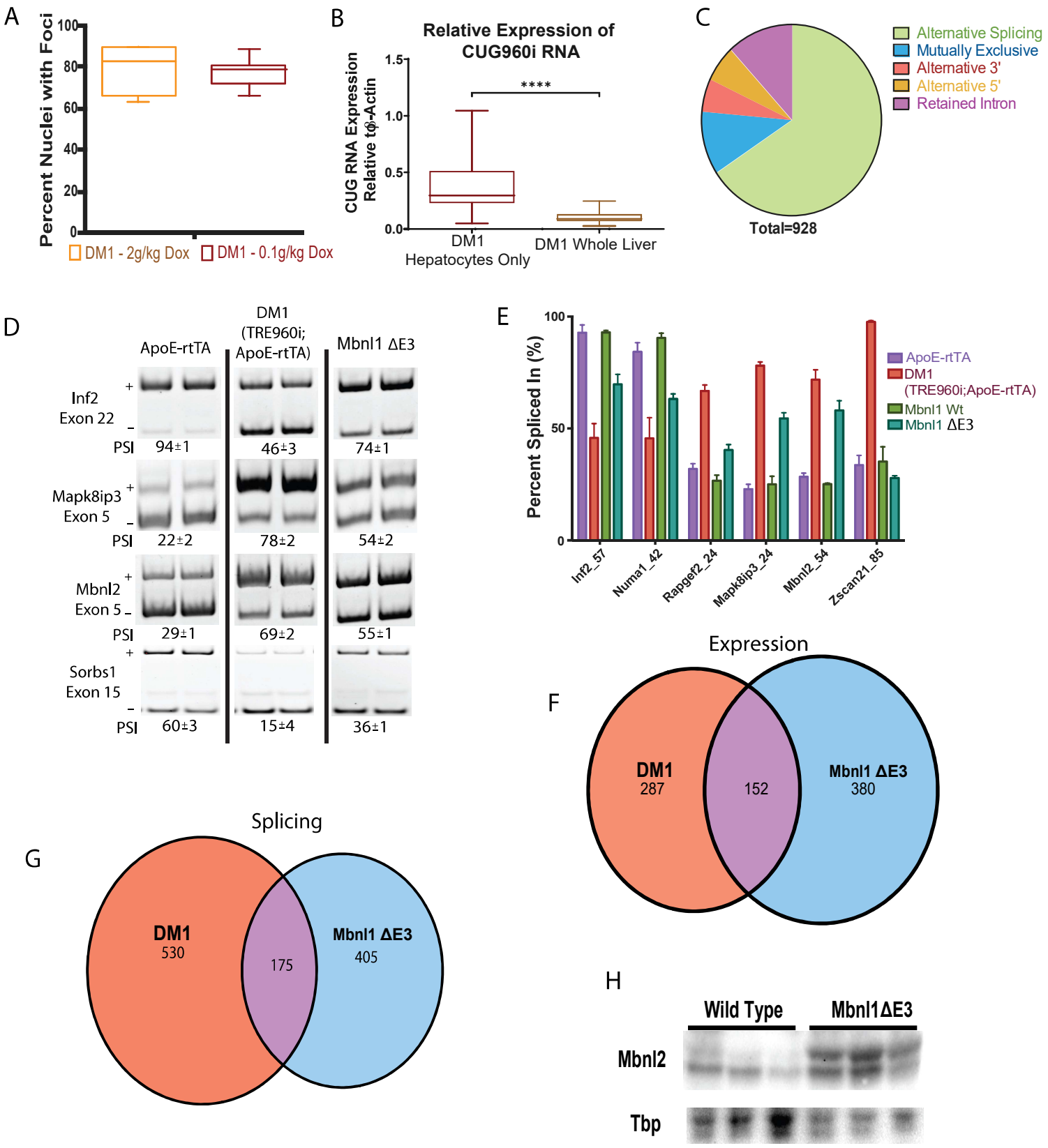

SUPPLEMENTAL FIGURE 2